

Gravity-Informed Deep Learning Framework for Predicting Ship Traffic Flow and Invasion Risk of Non-Indigenous Species via Ballast Water Discharge

Ruixin Song^{1,★}, Gabriel Spadon^{2,★}, Ronald Pelot³, Stan Matwin^{2,4}, and Amilcar Soares⁵

¹ Department of Computer Science, Memorial University of Newfoundland, St. John's – NL, Canada

² Institute for Big Data Analytics, Dalhousie University, Halifax – NS, Canada

³ Industrial Engineering Department, Dalhousie University, Halifax – NS, Canada

⁴ Institute of Computer Science, Polish Academy of Sciences, Warsaw, Poland

⁵ Department of Computer Science and Media Technology, Linnaeus University, Växjö, Sweden

★ These authors contributed equally to this work.

Corresponding author: gabriel@spadon.com.br

ABSTRACT

Aquatic invasive species are a significant threat to biodiversity and ecosystems worldwide. Due to the fast growth of global trade and transportation networks, non-native species have been introduced and spread unintentionally in new environments. These invasive species can damage ecosystems by disrupting the balance, out-competing native species, and causing significant economic losses to agriculture, forestry, and fisheries. Therefore, there is a pressing need for risk assessment and management techniques to mitigate the impact of these invasions. This study aims to develop a new physics-inspired model to forecast maritime shipping traffic and thus inform risk assessment of invasive species spread through global transportation networks. Inspired by the gravity model for international trades, our model considers various factors that influence the likelihood and impact of vessel activities, such as shipping flux density, distance between ports, trade flow, and centrality measures of transportation hubs. Additionally, by analyzing the risk network of invasive species, we provide a comprehensive framework for assessing the invasion threat level given a pair of origin and destination. Accordingly, in this paper, we introduce transformers to gravity models to rebuild the short- and long-term dependencies that make the risk analysis feasible. Thus, we introduce a physics-inspired framework that achieves an 89% segmentation accuracy for existing and non-existing trajectories and an 84.8% accuracy for the number of vessels flowing between key port areas, representing more than 10% improvement over the traditional deep-gravity model. Along these lines, this research contributes to a better understanding of invasive species risk assessment. It allows policymakers, conservationists, and stakeholders to prioritize management actions by identifying high-risk invasion pathways. Besides, our model is versatile and can include new data sources, making it suitable for assessing species invasion risks in a changing global landscape.

Introduction

Globalization has rapidly increased marine shipping activities in the last decades. According to a statistics report, container shipping has increased by 24 times in tonnage from 1980 to 2020¹. During this time, the environmental pollution caused by introducing Non-Indigenous Species (NIS) through shipping activities has been a subject of study regarding marine preservation. Ballast water, used to keep vessels in balance during travels, is listed as a major source of NIS pollution². The introduction of NIS into different ecological regions due to ballast water discharge has been shown to cause significant damage to the local ecosystem. It poses a severe threat to the biodiversity of affected areas. In response to biological invasion issues, many studies about Ballast Water Risk Assessment (BWRA) and tools have been developed over the last decades to estimate the risk levels of carrying NIS in the ballast water tanks³⁻¹³. These works and tools rely on ship self-reports, such as made available by the National Ballast Information Clearinghouse (NBIC)¹⁴. Ballast water reporting forms provide information on the water source and destination areas, allowing for an assessment of the environmental similarity between source and target locations of a vessel voyage, which is considered a significant indicator of invasion risk level². However, the acquisition of ballast reports is limited at the global scale due to the various policies across different countries. Additionally, BWRA lacks alternative sources that incorporate comprehensive shipping information.

Recent research has revealed a strong correlation between the introduction of non-indigenous species and the movement of ships through shipping networks. These studies^{12,15} have utilized data from the Automatic Identification System (AIS), a sophisticated location tracking system on ships that allows them to share their positions in real-time¹⁶. This technology allows researchers to track individual/collective ships¹⁷⁻²⁰, predict larger-scale shipping activities²¹, and assess the risk of introducing NIS through ballast water¹². AIS data has emerged as a promising source of information for studying bioinvasions in marine ecosystems. These studies analyze mobility flow by using Origin-Destination (OD) models that combine physics with statistical mechanics. The gravity model, inspired by Newton's *Law of Universal Gravitation*, measures the attractive force between two objects based on their masses and the distance between them²². The gravity-inspired OD models were introduced in early human mobility and migration studies^{23,24}. They rely on information about population size and distances between origins and destinations as features.

The gravity theory permeates many areas of study that go beyond mobility and migration, such as the spreading of epidemics^{25,26}, commercial trading²⁷, communication²⁸ and shipping networks^{15,29} modeling. Although the gravity model has been widely used to model real-world problems, recent studies have shown that it may not be sufficient for capturing complex patterns in various scenarios³⁰. Relying solely on mass and distance as the critical factors of the model could lead to failures in accurately representing patterns³¹. Nonetheless, the gravity model has been prevalent for many years and remains a popular tool for modeling various phenomena. Beyond gravity models, radiation absorption is another physics-inspired OD model to study mobility patterns³²⁻³⁴. Unlike gravity models, which draw inspiration from gravitational forces, radiation models are based on principles seen in radiation and absorption

processes, also from physics. While gravity models contain adjustable variables that may be difficult to define, the radiation-absorption model simplifies this by emphasizing distance as the primary feature while considering the population density. The well-known application of the radiation model is to predict human movement toward locations influenced by employment indicators³². Further studies used field theory for abstracting vector fields of daily commuting flows³⁵, while others translated field theory-based mobility to deep learning models for achieving better interpretation of spatiotemporal features in mobility patterns³⁶.

The deep learning techniques discussed above in the mobility domain are a subset of the machine learning realm, and they have become increasingly popular in various applications due to their ability to recognize patterns by fine-tuning multiple parameters. These techniques have been used to forecast vessel trajectories in the ocean, predict patient trajectories in hospitals, track the spread of epidemics, and many other applications³⁷⁻⁴⁰. Understandably, coupling machine or deep learning capabilities for pattern recognition with physics-inspired OD models can imply a higher proficiency in capturing and predicting complex scenarios. For instance, a study in human mobility used deep learning methods with the gravity model⁴¹. The resulting composite model called the Deep Gravity Model, has expanded the standard feature set of conventional gravity models, which typically incorporated population size and distance between OD locations, to include a variety of parameters characterizing the origins and destinations such as land-use patterns and the presence of retail and healthcare amenities. A similar study proposed the use of machine learning models augmented with urban indicators to forecast the flow of commuters during worker migrations⁴², which included data about labor, safety, and quality of life and work in the cities using censuses-collected data. The enriched feature set enabled both models to discern and capture the intricacies of human mobility across wider information spaces. Specifically, deep learning techniques have inherent learning mechanics characterized by feed-forward and feedback-connectivity. These mechanics allow for adaptive weight assignment to individual variables. Therefore, this blend of deep learning and traditional OD models sets a promising premise for its application in maritime traffic mobility networks, as it allows intricate exploration of patterns at a granular level required for shipping network analysis.

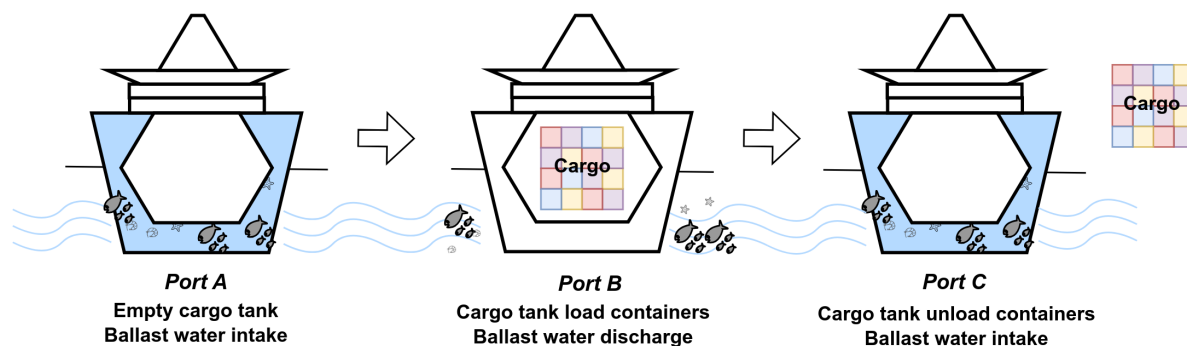


Figure 1. Non-indigenous species carried by ballast water during container shipping.

Along these lines, this paper focuses on predicting the OD fluxes of marine vessels to gain insight into global shipping behavior and their role in preventing NIS cases through BWRA. Ballast water is essential

in maritime operations, particularly for container ships. As illustrated in Figure 1, while ballast water helps stabilize the ship's load, local species can enter the ballast tanks and travel long distances when the water is taken in and discharged. Therefore, forecasting shipping patterns is critical to understanding the risk of spreading NIS. To this end, we propose a gravity-informed model where the shipping fluxes are considered as “mass”, and the vessel traffic flows are inversely proportional to the distances traveled by ships. We have enriched our model with relevant features from shipping activities, including bilateral trade data between countries⁴³ and graph metrics extracted from the global shipping network. Our deep learning model, known as the *Transformer Gravity*, relies on the transformer architecture⁴⁴ and is proficient in capturing local and global data dependencies through self-attention mechanisms. This mechanism enables the model to weigh the importance of different parts of the input sequence, assigning varying degrees of attention depending on the relevance of each input part during generating the output. As a result, our model can discern and incorporate short- and long-term dependencies in vessel traffic flows, making it more sensitive to the complex and dynamic patterns in maritime vessel movements.

As part of our proposed framework, we have employed a machine learning classifier that proceeds the flow estimation process and filters out non-existing edges on a link-prediction binary classification task, a two-stage modeling process. This allows only highly probable flows, based on prior knowledge, to be fed into the gravity-based models, where the final flow estimations take place with the aid of the gravity-based model. In this sense, we have conducted experiments using the (a) Transformer Gravity, (b) Deep Gravity, and (c) Shallow Gravity Models. We utilized regression models in machine learning for performance comparison, and the same approach was used regarding the binary classification task. Our results demonstrate that the Transformer Gravity model significantly outperforms all the other approaches as it achieves an average Common Part of Commuters (CPC) of 85.3%, representing an improvement higher than 10% in the model output certainty in contrast to the Deep Gravity counterpart and over 20% improvement compared to the Shallow Gravity and other regression models. The results we have obtained are due not only to the proposed model but also to the proposed pipeline. We have significantly improved performance by incorporating prior knowledge about potential destinations and using the attention mechanism and the traditional gravity-informed model for mobility flow estimation.

Overall, we provide a consistent advancement in the gravity-informed flow estimation models that paved the way for ballast water risk assessment and management by enabling the forecasting of vessel mobility flows. That was possible mainly due to advancements in the model pipeline and architecture, which strongly rely upon key ocean and vessel mobility domain features. Specifically, data from global economic trades between countries and graph centrality metrics from port networks significantly contribute to achieving state-of-the-art results. This emphasizes the value of integrating shipping network analysis and trade information into vessel mobility flow predictions. Although gravity-informed models have limitations in capturing temporal dynamics³⁰, the annual patterns in ship traffic flows predicted by the Transformer Gravity model can provide references for shipping intensity in ballast water risk assessment. In addition, due to the versatility of mobility data, we believe that our framework and model can be utilized

in various fields of research such as human mobility, urban transportation, and epidemic modeling.

Results

At the beginning of this study, we constructed a directed and weighted international shipping network based on global port visits data in the same way as in⁴⁵ from 2017 to 2019. Ports and shipping connections were represented as nodes and edges in the shipping network, and the World Port Index (WPI)⁴⁶ was also used for port identification. Figure 2 provides an overview of global shipping connections in the three years from 2017 to 2019 and the distribution of ports participating in these shipping activities.

Notice that, our study was conducted during a period of significant events (*e.g.*, war, global pandemic, and economic sanctions) that could have influenced the underlying shipping data. However, all results we discuss use the same methodology, ensuring that any external factors would have had a homogeneous impact on the comparative performance of the models, maintaining the integrity of our analysis and results.

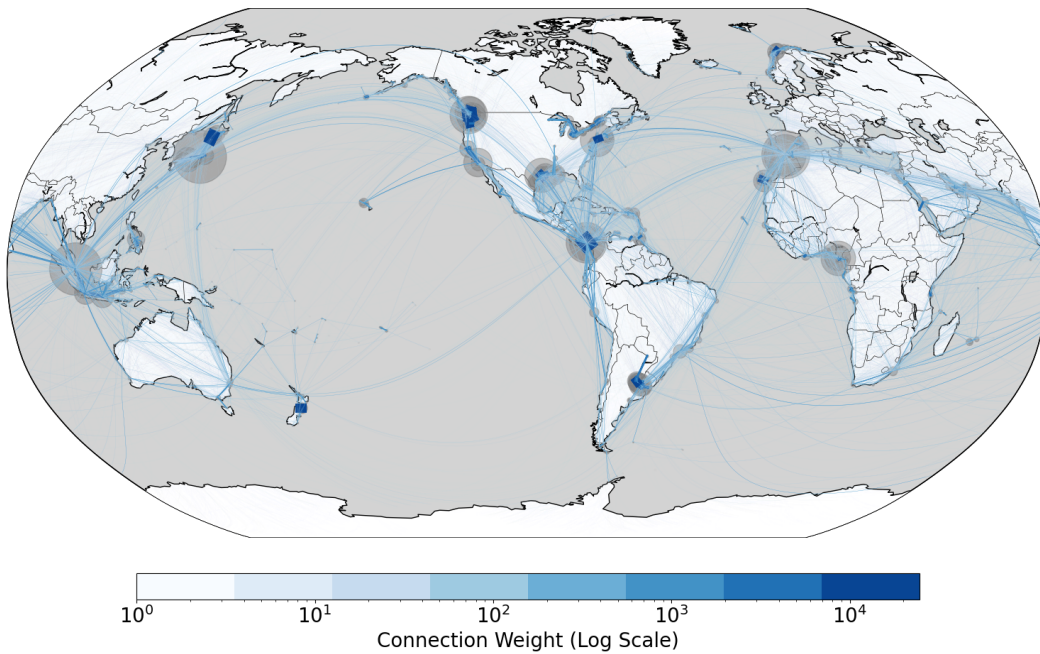


Figure 2. Global shipping network joining data from 2017 to 2019.

Global Shipping Network

The global shipping network can be described as $G = (V, E, W)$, where V represents the set of ports, E is the set of shipping routes connecting pairs of ports, and W is the collection of edge weights. In this context, each weight in W corresponds to the number of individual trips T_{ij} between port i and port j :

$$W = \{w_{ij} : w_{ij} = \sum_t T_{ij}(t) \forall (i, j) \in E\}$$

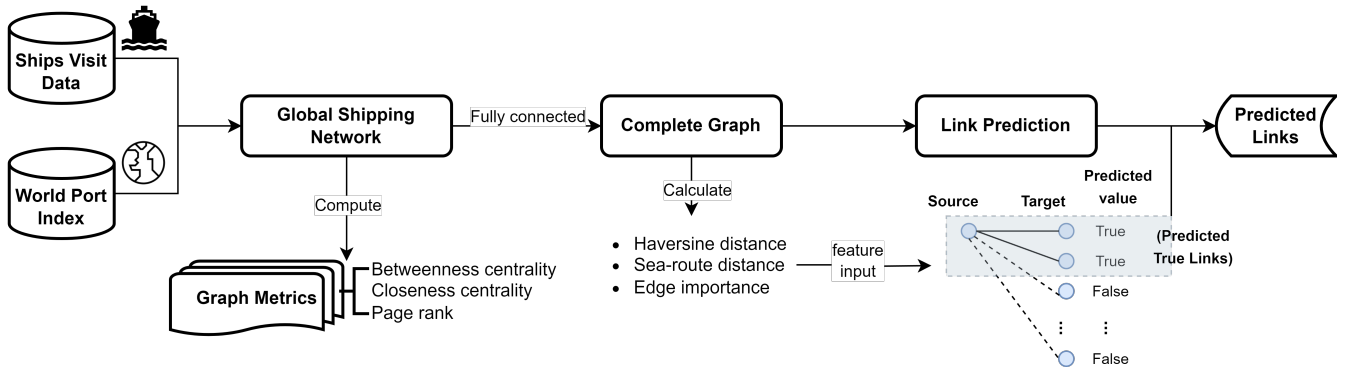


Figure 3. Pipeline for analyzing and predicting links in the global shipping network from 2017 to 2019.

With the global shipping network defined, we performed network analysis to extract graph metrics as features for our proposed gravity-informed predictive model. We also conducted link prediction to identify potential origin-destination (OD) pairs within current shipping traffic, thus providing pre-knowledge to the predictive models. Figure 3 illustrates the pipeline of shipping network analysis and the link prediction process, which precedes the gravity-informed predictive models forecasting the ship traffic flows.

Graph Metrics Computation

We analyzed the shipping network by calculating various graph metrics for each node. These metrics included betweenness centrality, closeness centrality, and PageRank. The detailed equations for calculating these metrics are listed in Equations 14, 16, and 17 in the Methods. In this paper, betweenness centrality quantifies the frequency with which a port serves as an intermediary on the shortest paths between other ports — ports with high betweenness centrality play a critical role as bridges within the shipping network. Additionally, closeness centrality calculates the inverse of the sum of the shortest distances from a node to all other nodes — ports with a high degree of closeness are easily accessible from all other ports in the shipping network. Furthermore, PageRank⁴⁷ identifies essential nodes in a graph — ports with high metric values are more influential and likely to be frequently visited by ships from other important ports.

After calculating three different graph metrics, we noticed that they all showed positive non-linear

Port Name	$C_B(i)$	$C_C(i)$	P_{ij}	Water Body	Country	Region
Keppel	0.021	0.562	0.012	Strait of Malacca	Singapore	South-eastern Asia
Europa Point	0.018	0.553	0.012	Strait of Gibraltar	Gibraltar	Southern Europe
Puerto Cristobal	0.018	0.539	0.007	Caribbean Sea	Panama	Latin America & Caribbean
As Suways	0.018	0.532	0.003	Gulf of Suez	Egypt	Northern Africa
Balboa	0.018	0.523	0.006	Gulf of Panama	Panama	Latin America & Caribbean

Table 1. Ports with the highest graph metric values in betweenness centrality ($C_B(i)$), closeness centrality ($C_C(i)$), and page rank (P_{ij}) with port information⁴⁶, including water body, country, and region.

correlations with each other. This means that as one metric increased, the others also tended to increase. Although each metric has a distinct interpretation, we found five ports from different bodies of water that had high values in all three metrics (see Table 1). These ports are particularly noteworthy because they excel in multiple areas. Many of the most influential ports are located at crucial marine traffic junctions that connect different oceans, such as the Gulf of Suez, the Gulf of Panama, and the Strait of Malacca.

Link Prediction in the Shipping Network

Subsequently, during the shipping network analysis, we observed the presence of disconnected components. These disconnected segments pose a challenge for our proposed framework, which relies on integrating features across all possible destinations from each source port. Such disconnections can compromise the model’s ability to generate accurate or well-defined predictions for shipping flows between isolated areas. Thus, we transformed the original network into a complete graph, denoted as G' , and assigned a small value to weigh the new links. This action mitigates the issues arising from data sparsity and establishes a uniform data structure, thereby enhancing the robustness of the flow estimation framework. With the fully connected shipping network G' , we proceed with the flow estimation framework by forecasting whether a trajectory exists by solving a link prediction problem in G' , which can be framed as a binary classification task within machine learning models. This action gives concrete source-destination pairs well-prepared for building feature sets, modeling the gravity structure, and introducing the deep learning framework.

To perform link prediction, we first separated the shipping data from 2019 for testing and retained the data from 2017 and 2018 for training and validation. Then, we prepared features for the classification task. We calculated the Haversine distances (see Methods) between every pair of ports. However, Haversine distances only provide the geodesic approximation and cannot capture the real sea routes that the ships have traveled. Therefore, we also computed the sea-route distances between port pairs and obtained a more accurate representation using a Python package that models the shortest routes and calculates the sea route distances using historical trajectories⁴⁸. Finally, we used these distances to evaluate the importance level I_{ij} for each edge $\langle i, j \rangle$ in the complete graph G' . Inspired by straightness centrality measuring the node connectivity by the straightness of the shortest distance⁴⁹, this metric combines the normalized flow size \hat{w}_{ij} and the normalized Haversine distance \hat{d}_{ij}^E , using a small constant ϵ to prevent division by zero. Connections with more shipping flows and shorter distances are considered more important:

$$I_{ij} = \frac{\hat{w}_{ij}}{\hat{d}_{ij}^E + \epsilon}, \quad i, j \in V', \quad i \neq j \quad (1)$$

Next, we incorporated the Haversine distance, sea route distance, and edge importance into the feature set to determine the existence of a trajectory between two ports. Upon labeling the real (true class) and pseudo (false class) links in the complete network G' , we observed a significant class imbalance (2.3% real links and 97.7% pseudo links); consequently, we employed stratified sampling of the pseudo links based on their spatial distribution to balance the number of examples in each class in a manner that preserved the data’s characteristics. Machine learning models were then engaged to perform binary classification,

utilizing 75% of data from 2017 and 2018 for training and 25% for validation. During the training phase, a 5-fold grid search cross-validation was implemented to fine-tune the hyperparameters of each model. Finally, we tested the models on unseen data from 2019, reinforcing the validity of our approach.

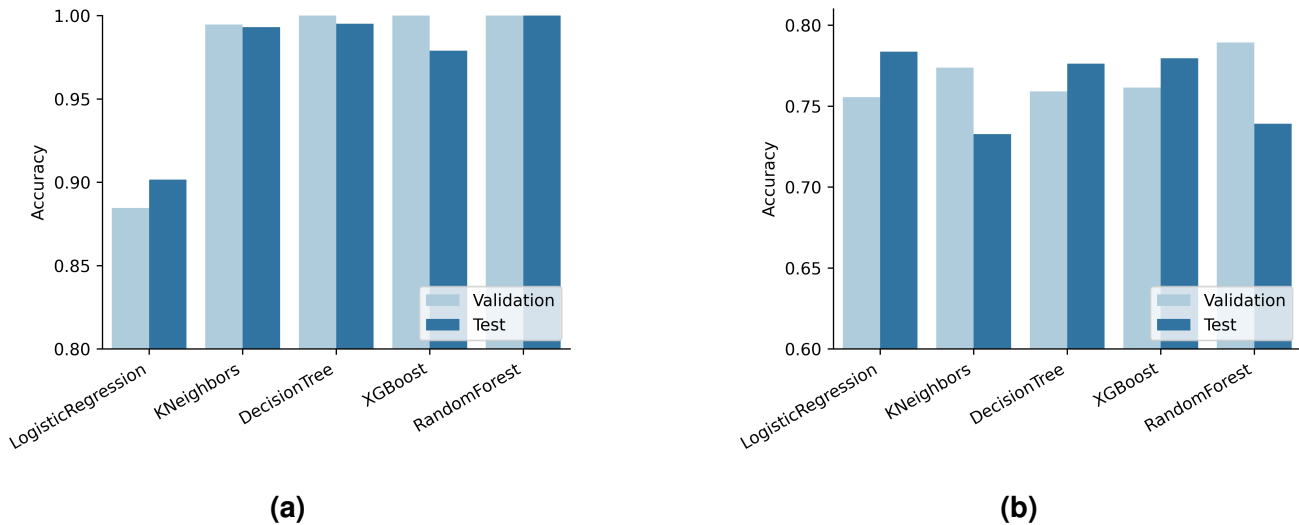


Figure 4. validation and test accuracy of classifiers in the trajectory link prediction task. (a) Performance of the classification task incorporates Haversine distance, sea route distance, and edge importance as features. (b) Performance of classification task without the edge importance features.

Figure 4a displays the validation and test accuracy across different classification models. It can be observed that apart from Logistic Regression at 89%, all other models achieved high accuracy (above 98%) on both the validation and the test datasets. We further investigated the discrepancies between the model with the highest performance (Random Forest at 100%) and the model with the lowest accuracy (Logistic Regression at 89%). The result revealed that the links primarily missed by Logistic Regression were those with only 1 or 2 trips and, to a lesser extent, 3-trip links. We also observed that the high accuracy of some models could be attributed to the inclusion of normalized edge weights w_{ij} in G' (*i.e.*, the normalized number of trips) in the edge importance calculation as per Equation 1. Consequently, we ran predictions without edge importance as a feature to mitigate this effect for comparison. Figure 4b presents the validation and test accuracy when relying solely on Haversine and sea route distance as features. The accuracy of these models ranges from 75% to 79%. Notably, the models' performance decreases by 16% to 20% compared to models that use edge importance as a feature. Retaining critical details from trade fluxes directly proportional to the link's existence is the key function of the edge importance feature. However, we have observed that more than the edge importance is needed to create a self-contained inference model. The challenge lies in selecting a model that can utilize the extra information without overfitting the data.

After analyzing the results from the model shown in Figure 4a, we observed that the Random Forest model has a higher accuracy. However, the Logistic Regression model acts as a filter by removing some 1- and 2-trip trajectories before predicting ship traffic flow. These trajectories are considered unstable and

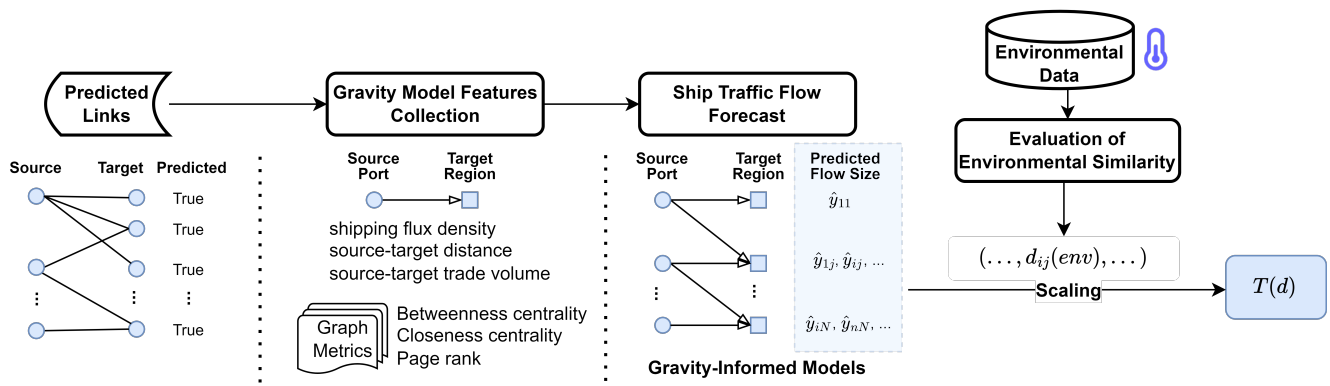


Figure 5. Experimental pipeline for predicting ship traffic flows with gravity-informed models and assessing environmental similarity for ballast water risk assessment (continuation from Figure 3).

unreliable for predicting future mobility flow and may be outliers. Therefore, the Logistic Regression model is used to identify and remove these trajectories, leaving behind only those predicted to have more stable traffic flow between origin-destination pairs. These trajectories are then utilized as features of gravity-informed models for improving ship traffic flow prediction, such as seen in Figure 5, which allows for the environmental similarity analysis and the ballast water risk assessment discussed as follows.

Gravity Model

As in the laws of gravity, the gravity model describes the interaction between two entities proportionally to their masses and inversely proportional to their distance²². Over time, the model has been adapted to solve various practical problems, such as application in studying human mobility and migration patterns^{23,24}, which follows the gravity basis that the number of commuters between two locations is related to the populations of the two locations and the physical distances. In addition, the gravity model also includes adjustable parameters that can be learned from historical data. Other popular applications include forecasting economic interactions²⁷, communication networks²⁸, and cargo shipping^{15,29,50}.

Even though the gravity model has prevailed for many years, its limitations can hardly be overlooked. First, the simple components of “masses” and “distances” cannot capture the connection with real mobility flows and lack comprehensive factors that can represent specific scenarios³², such as the city infrastructure in urban mobility studies and the global trade pattern impacting cargo shipping flows. Also, the lack of limits on the flow increase can lead to the predicted flow size larger than the source “masses”, making the model predictions unreasonable and challenging to interpret^{32,42}. Additionally, it is difficult to deal with multiple adjustable parameters in the model for the prediction without enough previously observed data.

Alternative solutions have been proposed to overcome the limitations of gravity models in predicting mobility flows. In this sense, the radiation model offers a parameter-free approach which resolves the problem of having multiple parameters in the gravity model. Besides, it limits the number of flows by introducing the total number of individuals departing from the source location^{32,34}. Moreover, different

studies used multiple relative factors, such as employment and urban infrastructure, that capture more important characteristics to improve prediction accuracy and adaptability of the model^{41,42}. The evolving nature of artificial intelligence and the rise of large language models have brought about new technologies. Therefore, improving the state of the art by using more capable technologies over new arrangements and combinations of data is essential. This becomes more evident when considering evolving factors such as climate change and recurrent anthropogenic effects observed on the oceans.

Traditional Deep Gravity

Deep Gravity is a recent study in urban mobility that integrates the gravity model with deep neural networks⁴¹. Unlike traditional gravity models that rely on maximum likelihood estimation for parameter tuning, Deep Gravity utilizes a cross-entropy loss function as a substitute for maximum likelihood estimation. This innovative approach effectively adapts the gravity model to a neural network framework. Also, it departs from the traditional multi-parameter structure of gravity models; instead, it incorporates the populations, distances, and infrastructures into the feature set and integrates data from various sources.

However, the simplicity of the multilayer perceptrons (MLPs) structure in Deep Gravity presents certain limitations. Specifically, the complex multivariate relationships inherent in mobility flows can be challenging to capture accurately through the composition of multiple linear functions. Moreover, the deep architecture composed of fifteen linear layers stacked in sequence demands many model parameters. Thus, it requires more computational resources and training time to provide a viable solution. While Deep Gravity utilizes a multilayer architecture, the underlying gravity model can be simplified to contain one or a couple of layers. In this study, we employed multiple multi-layered models as benchmarks for comparison against our proposed framework that leverages Transformers on Deep Gravity Models.

Transformer Deep Gravity

In this study, we incorporate the self-attention mechanism of the Transformer architecture⁴⁴ into our proposed framework. Compared to the conventional MLPs structure, the self-attention mechanism can inspect the input sequence and weigh to identify and prioritize the most relevant elements for generating the output, and this characteristic enables our model to capture crucial dependencies in vessel mobility flows effectively. Additionally, the self-attention mechanism accomplishes high performance with fewer parameters, making it a computationally efficient model. This section shows how we model the *Transformer Gravity*, combining the characteristics of the Gravity Model and the self-attention mechanism.

Problem Definition

Based on the pairs of source-destination ports obtained from the previous link prediction step, we encode the destination ports into 17 geographical regions according to the ISO-3166 standard⁵¹, where ports within regions are expected to have a similar set of organisms and, therefore, share similar habitat. Over the encoded representation of regions, we now aim to estimate the sizes of shipping mobility flows between each source-destination pair (P_i, P_j) , where P_i is the source port and P_j is the destination port that pertains

to a unique geographical region. A ship departing from a source port may have one or more destination ports in the same or different regions, and following the Deep Gravity⁴¹ method, the goal is to estimate probabilities of the ships traveling to these geographical regions, becoming a multiclass classification task.

Predict target: We compile a set of 10 features from various sources for each pair (P_i, P_j) , such as shipping fluxes at ports, geodesic distances between source and destination, global economic trade volume, the graph metrics computed with the global shipping network, and others; detailed information about these extracted features is provided in Table 3 in the Methods. We represent the feature vector for each source-destination pair as $x_{ij} = \langle m_1, m_2, \dots, m_{10} \rangle$. Given the ships from each source port travel to multiple destination regions, these feature vectors are aggregated into a single data sample $X_i = \{x_{i1}, x_{i2}, \dots, x_{iN}\}$, where N is the number of destination regions in the data sample, and $1 \leq N \leq 17$. Each destination region is represented as a class, so the prediction has N classes for a sample. Since samples of varying lengths cannot be wrapped to a tensor for batch processing, we set the batch size to 1 for model input. Using \hat{y}_{ij} as the estimated size of the mobility flow between (P_i, P_j) , which is the target of the prediction, we have:

$$\hat{y}_{ij} = O_i \cdot p_{ij} \equiv O_i \frac{e^{f(x_{ij})}}{\sum_{k=1}^N e^{f(x_{ik})}} \quad (2)$$

where O_i represents the total number of ships departing from source port i . p_{ij} is the probability of ships traveling from source port i to the destination region j , and $f(x_{ij})$ is the model output of feature vector x_{ij} .

Loss function: We used the cross-entropy loss function for the model optimization process, defined as:

$$L(\hat{y}_{ij}, y_{ij}) = - \sum_{i=1}^M \sum_{j=1}^N y_{ij} \cdot \ln \left(\frac{e^{f(x_{ij})}}{\sum_{k=1}^N e^{f(x_{ik})}} \right) = - \sum_{i=1}^M \sum_{j=1}^N y_{ij} \cdot \ln \left(\frac{\hat{y}_{ij}}{O_i} \right) \quad (3)$$

The function presents the total loss between the predicted flows \hat{y}_{ij} , and the real flows y_{ij} for all the N destination regions from M source ports. The *log-softmax* function is applied to the model output $f(x_{ij})$, and the loss function in terms of p_{ij} is obtained by replacing the log-term by Equation 2 divided by O_i .

Evaluation metric: The *Common Part of Commuters* (CPC)⁵²⁻⁵⁴ is designed to measure the similarity between two sets of data, which could represent various aspects such as the volume of commuters, traffic, or trade between different locations. The metric calculates how much overlap there is between the predicted values \hat{y}_{ij} and the actual values y_{ij} . In the context of Equation 4, M represents the number of source ports and N the number of destination regions. The values \hat{y}_{ij} and y_{ij} correspond to the flow of vessels from source port i to destination region j , based on a model's prediction and the actual observed values, respectively. A high value of the CPC, in this case, means that there is a large overlap between the predicted and actual datasets. Specifically, it would indicate that the predictions accurately capture the true data distribution patterns, with most predictive quantities closely matching the actual quantities. Contrarily, a low value of the CPC would suggest that there is little overlap between the predictions and the actual data, indicating that the model's predictions diverge significantly from the observed data, which could be due to underprediction or overprediction in various parts or a general misalignment of the model

with the reality. Accordingly, CPC considers the minimum common value between the predicted and actual data for each pair of source and destination ports, measuring the intersection over the values union:

$$CPC(\hat{y}_{ij}, y_{ij}) = \sum_{i=1}^M \frac{2 \sum_{j=1}^N \min(\hat{y}_{ij}, y_{ij})}{\sum_{j=1}^N \hat{y}_{ij} + \sum_{j=1}^N y_{ij}} \quad (4)$$

For a better evaluation process, besides the CPC, we included the Normalized Root Mean Square Error (*NRMSE*) — lower is better — and Pearson Correlation Coefficients (*Corr.*) — higher is better — to measure the normalized errors and the correlation between the predictions and observations, defined as:

$$NRMSE(\hat{y}_{ij}, y_{ij}) = \sum_{i=1}^M \frac{\sqrt{\frac{1}{N} \sum_{j=1}^N (y_{ij} - \hat{y}_{ij})^2}}{\max(y_{ij}) - \min(y_{ij})} \quad (5)$$

$$Corr.(\hat{y}_{ij}, y_{ij}) = \sum_{i=1}^M \frac{\sum_{j=1}^N (y_{ij} - \bar{y}_{ij})(\hat{y}_{ij} - \bar{\hat{y}}_{ij})}{\sqrt{\sum_{j=1}^N (y_{ij} - \bar{y}_{ij})^2 \sum_{j=1}^N (\hat{y}_{ij} - \bar{\hat{y}}_{ij})^2}} \quad (6)$$

Model Framework

Our proposed Transformer Gravity model is composed of three main components: (1) the input embedding layer, which maps the input feature vectors to a higher-dimensional space that is compatible with the Transformer architecture; (2) the multilayer Transformer encoder, which involves the self-attention and feed-forward blocks that process the embeddings to capture complex relationships between input features; and, (3) the output linear layer, which maps the processed embeddings to the target flow predictions, computes loss and CPC and performs backpropagation based on the loss values. Figure 6 presents the model pipeline using two stacked Transformers modules and provides a glance at the layer's relationships.

Linear Embedding. The embedding layer takes the input sample, which is a sequence of feature vectors represented as $\{x_{i1}, x_{i2}, \dots, x_{iN}\}$. It then maps each vector into a higher-dimensional space using a linear transformation that involves a weights matrix and a bias vector. The result of this transformation is the feature embedding \mathbf{z}_0 for each vector x_{ij} , which can be obtained following the subsequent calculation:

$$\mathbf{z}_0 = x_{ij} \cdot W_0^\top + b_0, \quad x_{ij} \in \mathbb{R}^{1 \times n}, \quad W_0 \in \mathbb{R}^{d \times n}, \quad b_0 \in \mathbb{R}^{1 \times d} \quad (7)$$

The input vector x_{ij} with 10 features is represented by W_0 (the weight matrix) and b_0 (the bias vector). This input vector is then embedded into a 64-dimensional space, resulting in an embedded output $\mathbf{z}_0 \in \mathbb{R}^{1 \times d}$. Subsequently, the embedded output is passed to the multi-head attention encoder layers as the input.

Multi-Head Attention. A multi-head attention encoder comprises a multi-head self-attention mechanism and a feed-forward network, followed by layer normalization (as illustrated in Figure 6). Within each self-attention head, the input \mathbf{z}_0 is transformed into queries Q_h , keys K_h and values V_h using the weight matrices W_Q , W_K and W_V , respectively. Self-attention then calculates $Head_h = softmax\left(\frac{Q_h \cdot K_h^\top}{\sqrt{d_k}}\right) \cdot V_h$,

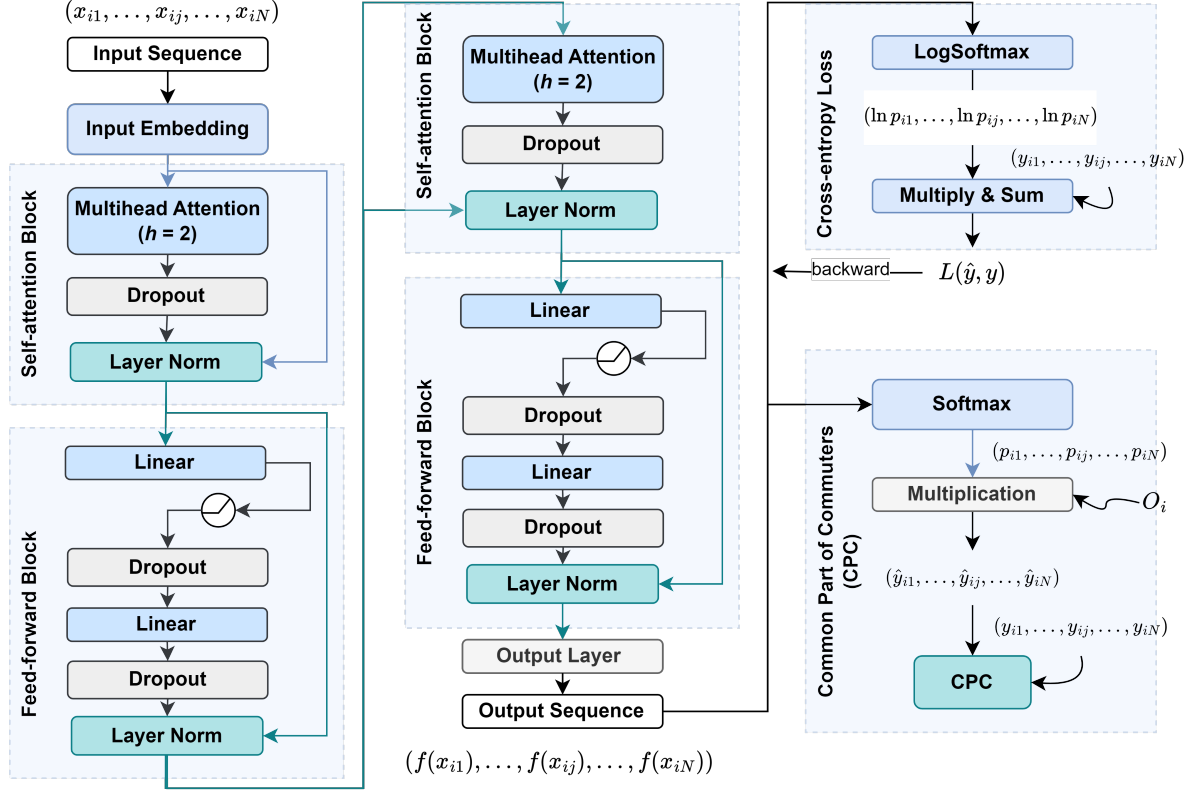


Figure 6. Framework of the Transformer Gravity model.

where $d_k = \frac{d}{h}$ is the dimension of the queries Q_h and keys K_h and is used to scale the product $Q_h \cdot K_h^\top$. Multi-head attention combines all heads and linearly transforms the concatenation to produce $\mathbf{z}_1 \in \mathbb{R}^{1 \times d}$:

$$\mathbf{z}_1 = \text{Concat}(\text{Head}_1, \dots, \text{Head}_h) \cdot W_C, \quad W_C \in \mathbb{R}^{hd_v \times d} \quad (8)$$

In our experiment, we define the number of heads as $h = 2$, and the heads run operations in parallel.

Layer Normalization. After the multi-head attention layer, there is a dropout layer that randomly sets a certain percentage of elements to 0. The dropout ratio p is set to 0.1 as per Equation 9. Next, a skip connection is applied to add the input features \mathbf{z}_0 to the output of the dropout layer $\mathbf{z}_{dropout}$ before the self-attention block. This helps to retain the information from the input features and prevent vanishing gradients during backpropagation. The output of this connection, \mathbf{z}_{skip} , is then normalized using Equation 9, where μ is the mean and σ is the standard deviation of \mathbf{z}_{skip} with a small bias. The affine parameters α and β are initialized as 1 and 0, respectively, and can be optimized during the training process.

$$\begin{aligned} \mathbf{z}_{skip} &= \mathbf{z}_0 + \mathbf{z}_{dropout} \equiv \mathbf{z}_0 + \text{Dropout}(\mathbf{z}_1, p) \\ \mathbf{z}_2 &= \text{LayerNorm}(\mathbf{z}_{skip}) \equiv \frac{\mathbf{z}_{skip} - \mu}{\sigma} \times \alpha + \beta \end{aligned} \quad (9)$$

Feed-Forward Network. After the multi-head attention block processes the input, the resulting output is fed into a feed-forward neural network composed of an MLP structure. The connectivity of each layer

in the feed-forward block’s structure is illustrated in Figure 6. We formulate the output vectors from the layers using corresponding weight updates in Equation 10. Similar to \mathbf{z}_{skip} , a skip connection adds the vector \mathbf{z}_2 to the output \mathbf{z}_4 to preserve information from the self-attention block.

$$\begin{aligned}\mathbf{z}_3 &= Dropout \left(ReLU(\mathbf{z}_2 \cdot W_1^\top + b_1), p \right) \\ \mathbf{z}_4 &= Dropout \left((\mathbf{z}_3 \cdot W_2^\top + b_2), p \right) \\ \mathbf{z}_5 &= LayerNorm(\mathbf{z}_4 + \mathbf{z}_2)\end{aligned}\tag{10}$$

Training and Optimization. Our Transformer Gravity model has three transformer encoder layers stacked together to capture complex input embedding dependencies, but the number of stacked layers can be changed to match different requirements and needs. The output value \mathbf{z}_5 is obtained by passing the output of Equation 10 through a second and later third multi-head attention and feed-forward network block. The output value of the model is denoted as $f(x_{ij})$, and it produces a sequence of output values for a single data sample with a length of N . This sequence is then applied to a *softmax* function to produce probabilities $\{p_{i1}, p_{i2}, \dots, p_{ij}, \dots, p_{iN}\}$ for N classes. The predicted flow sizes $\{\hat{y}_{i1}, \hat{y}_{i2}, \dots, \hat{y}_{ij}, \dots, \hat{y}_{iN}\}$ for each destination are obtained by multiplying these probabilities with the total outflows O_i from the source port, as given in Equation 2. The loss for every sample is computed using Equation 3, and these losses are collected to derive the total loss. The model’s parameters are updated with each loss by processing a single sample. The summed CPC across all samples is calculated using Equation 4. After each training epoch, the summed CPC is divided by the number of samples M (*i.e.*, the number of source ports) to obtain the average CPC of that epoch. During training, we used the Adam optimizer with L_2 regularization on the weights and reduced the learning rate by a factor of 0.1 when there was no improvement with the validation CPC after 10 epochs. We applied early stopping when there was no improvement with the validation CPC after 20 epochs to prevent overfitting and improve training efficiency.

Experimental Results

During the experimentation, we used the proposed Transformer Gravity model with 1, 3, and 5 Transformer layers. This study compared the original 15-layer Deep Gravity model with a multi-layered variant of 3, 9, and 12 layers known as the Shallow Gravity models. Additionally, we experimented with machine learning regression models, such as linear-based, tree-based, and boosting-based models, as detailed in Table 2. The data from 2017 and 2018 formed the training data, while the 2019 data was used for testing.

Table 2 shows the mean, maximum, and minimum values of the models’ CPC across the five validation folds. Our proposed Transformer Gravity, particularly the ones with 3 and 5-layer configurations, have achieved the best performance in cross-validation with a mean CPC of 0.864, which marks a 10.5% improvement over the top-performing 3-layer Deep Gravity variant (CPC of 0.782), and a 13.2% improvement compared to original Deep Gravity model (CPC of 0.763) and over 49.7% to other machine learning models, whose mean CPCs ranged from 0.474 to 0.577. Meanwhile, we noticed that compared with the original Deep Gravity model, its shallower-layered variants show a better performance, evidenced

by metrics in both validation and test. However, none of these Deep Gravity variants can exceed the lowest mean CPC performance (CPC of 846 using a single layer) of the Transformer Gravity model. The gap between Transformer Gravity’s performance and other models indicates that our model’s predicted shipping flows have a larger resemblance to the real shipping flows, highlighting our model’s ability to reflect the real shipping mobility flows. This high similarity is also reflected in the other two metrics, $NRMSE$ and $Corr.$ The 3-layer Transformer Gravity model achieved the lowest error rate ($NRMSE$ of 0.080) and the highest correlation ($Corr.$ of 0.977) with actual shipping flows. These results suggest the Transformer Gravity model’s superior performance in predicting global ship traffic flows over the Deep Gravity model.

Model Name	Layers	5-Fold Cross-Validation					Testing			Parameters
		CPC_{mean}	CPC_{max}	CPC_{min}	$NRMSE$	$Corr.$	CPC	$NRMSE$	$Corr.$	
Linear Regression	—	0.474	0.564	0.353	0.327	0.457	0.570	0.327	0.563	—
Decision Tree	—	0.518	0.625	0.438	0.404	0.370	0.644	0.398	0.517	—
Random Forest	—	0.577	0.685	0.504	0.309	0.545	0.675	0.285	0.692	—
Extra Tree	—	0.573	0.686	0.483	0.311	0.535	0.699	0.255	0.767	—
Gradient Boosting	—	0.557	0.654	0.490	0.306	0.555	0.654	0.295	0.665	—
XGBoost	—	0.552	0.696	0.463	0.320	0.521	0.664	0.282	0.702	—
LightGBM	—	0.574	0.706	0.482	0.307	0.554	0.684	0.279	0.707	—
CatBoost	—	0.559	0.674	0.472	0.311	0.544	0.654	0.288	0.683	—
Deep Gravity ⁴¹	3	0.782	0.797	0.766	0.209	0.833	0.787	0.238	0.802	52,353
Deep Gravity ⁴¹	9	0.769	0.776	0.751	0.220	0.812	0.783	0.243	0.797	249,985
Deep Gravity ⁴¹	12	0.767	0.775	0.756	0.219	0.814	0.790	0.239	0.803	348,801
Deep Gravity ⁴¹	15	0.763	0.778	0.729	0.222	0.808	0.752	0.273	0.747	447,617
Transformer Gravity [★]	1	0.846	0.856	0.829	0.161	0.898	0.834	0.200	0.865	51,212
Transformer Gravity [★]	3	0.864	0.870	0.852	0.080	0.977	0.848	0.187	0.882	101,644
Transformer Gravity [★]	5	0.864	0.871	0.856	0.107	0.953	0.836	0.208	0.858	152,076

Table 2. Performance evaluation of the Transformer, Deep and Shallow Gravity models, and other baseline models. The cross-validation results present the mean (CPC_{mean}), maximum (CPC_{max}), minimum (CPC_{min}), mean Normalized Root Mean Square Error ($NRMSE$), and the mean Pearson Correlation Coefficients ($Corr.$) across five folds. Test results show the performance of the trained models on the entire test dataset. Details on the number of layers and parameters are provided for each deep learning model.

After analyzing CPC values in Table 2, it can be observed that the Transformer Gravity models show a more stable performance than the competing models. The difference between the highest and lowest CPC values for the Transformer Gravity models ranges from 0.015 to 0.027, which is lower than other gravity-based models (0.019 ~ 0.049) and machine learning models (0.164 ~ 0.233). This indicates that the variance in CPC is lower when the flow prediction is done with the Transformer Gravity model. The variance can be attributed to the distribution of data samples across folds, as a random seed is set

for the sample assignment. This way, the Transformer Gravity model’s performance is more consistent across different folds, meaning that given historical shipping data within the same temporal period, the Transformer Gravity model is more likely to predict shipping traffic flows with stable performance, regardless of the shipping traffic from which subsets of the data are sampled from.

On the right side of Table 2, we show the test results obtained by models trained on all the data from 2019 at once. The best *CPC* was produced by the 3-layer Transformer Gravity model (*CPC of 0.848*), which indicates that the overlap ratio between predicted and actual shipping traffic flows was very high for an unseen scenario that spanned a year. This benefits us, as it helps us obtain more accurate shipping patterns, which we can use to evaluate the shipping intensity for ballast water risks in the future. Moreover, our Transformer Gravity model had a Pearson Correlation Coefficient of 0.882. This value indicates a strong linear relationship between predicted and actual flows, demonstrating the model’s performance.

Table 2 shows that several baseline models have higher test *CPCs* than their best cross-validation *CPCs*. This difference in performance can be attributed to the distinct feature distributions in the test data compared to the cross-validation fold data. Additionally, the spatial and temporal dependencies intrinsic to the shipping data can also affect these evaluation results. Our training set includes shipping data from 2017 and 2018, while the test set comprises the entire year of 2019. Since both data sets represent complete years, the test data is expected to be more closely aligned with the training data in spatio-temporal distribution. This similarity can potentially explain the higher test performance than the validation results observed for these models. However, the evaluation of the Transformer Gravity model shows a better result in validation sets, which follow a more conventional pattern and have minimal variance over the cross-validation folds. This suggests that our model has learned more intrinsic connections from data features and is robust enough to overcome the impact potentially caused by the different distributions of datasets, demonstrating the model’s generalizability and reliability in predicting mobility flow patterns.

Table 2 also reveals that the performance of the Transformer Gravity model varies with the addition of layers. An increase in the number of the Transformer encoder layers initially enhances the model’s performance, as evidenced by the results of the 3-layer Transformer Gravity model compared with the single-layer model shown in the table. However, this performance increase is not unlimited. Comparing the 3-layer Transformer Gravity with the 5-layer one, as the model grows deeper with more integrated parameters, its performance tends to reach a plateau. Therefore, while stacking Transformers can be beneficial, it is important to optimize the number of layers to maximize the model’s performance.

Similarly, the Deep Gravity model also needs an optimized configuration. The original 15-layer Deep Gravity model includes 256 hidden dimensions for layers 1 to 5 and 128 dimensions for layers 6 to 15. Due to the relatively large performance variation among its validation folds (*CPC_{max} of 0.778* and *CPC_{min} of 0.729*), we adjusted the number of layers and experimented with shallower versions of the model for comparison. We followed the 1:2 ratio of the 256 and 128 dimensions in the original Deep Gravity to configure the 3, 9, and 12-layer variants. As per Table 2, we observed that Deep Gravity models with fewer layers delivered better performance than the original deep-layered model consisting of 15

layers. However, the performance of Deep Gravity models decreased with adding more layers. The 3-layer model of Deep Gravity performed the best, while deeper networks could not yield better results.

Risk Assessment of NIS through Ballast Water

As part of our study, we conducted a final experiment using the models we proposed on the global shipping network. Our goal was to assess the risk of NIS invasion associated with shipping flows using the BWRA decision tool, also employed by Transport Canada¹¹. We aimed to demonstrate how our proposed model can improve real-world risk analysis, providing better information for regulating the oceans and making policies. The tool takes into consideration environmental conditions such as sea surface temperature and salinity at the locations where ballast water is taken and discharged. We gathered environmental variables, including minimum, maximum, and annual temperature, and annual salinity at these locations, and compiled them into a vector called $\mathbf{v}_i = \langle t_{(i)_{min}}, t_{(i)_{max}}, t_{(i)}, s_{(i)} \rangle$. Through the vector \mathbf{v}_i , we proceed to calculate the environmental distance using the element-wise Euclidean distance calculation:

$$d_{ij}(env) = \sqrt{\sum_{k=0}^{|\mathbf{v}|} (\mathbf{v}_{i_k} - \mathbf{v}_{j_k})^2} \quad (11)$$

Based on Equation 11, a smaller $d_{ij}(env)$ value suggests a higher environmental similarity between the origin and destination, typically meaning a higher risk of NIS invasion via ballast water and vice versa.

Following the approach described above, we first integrated port data from *World Port Index*⁴⁶ with the environmental conditions in *Global Port Environmental Data*⁵⁵ to match the environmental variables with the ports. We then assigned these variables to each port involved in the ship movement of 2019, thus forming the environmental vector pairs $(\mathbf{v}_i, \mathbf{v}_j)$ for each pair of sources and destinations. Using Equation 11, we calculated the environmental distances for these pairs. In order to account for the differences in environmental distances across the shipping network, we included the frequency of each computed distance. This frequency is directly proportional to the predicted size of the shipping flow, which helps to adjust the environmental distance data to match the volume of shipping traffic. As illustrated in the pipeline diagram (Figure 5), we scaled the environmental distances using shipping volume from the Transformer Gravity model (denoted as $T(d)_{TG}$), the Deep Gravity model ($T(d)_{DG}$) and compared these with the scaled environmental distances based on actual shipping flows from 2019 (represented as $T(d)_{true}$). This approach was used to evaluate the dissimilarity of risk assessment results associated with the predicted and real shipping flows.

Figure 7 shows the distributions of the three distance groups: $T(d)_{true}$, $T(d)_{TG}$, and $T(d)_{DG}$, from which we can find that $T(d)_{true}$ and $T(d)_{TG}$ are closely aligned in their trends, even in minor fluctuations. In contrast, $T(d)_{DG}$ is more differentiated from $T(d)_{true}$. To quantify the alignment between $T(d)_{TG}$ and $T(d)_{true}$, we calculated Pearson's correlation coefficients for the two groups of environmental distances, reaching the value of 0.889. This high coefficient indicates a strong linear correlation between the environmental distances associated with actual and predicted shipping flows. Figure 7 also reveals that the

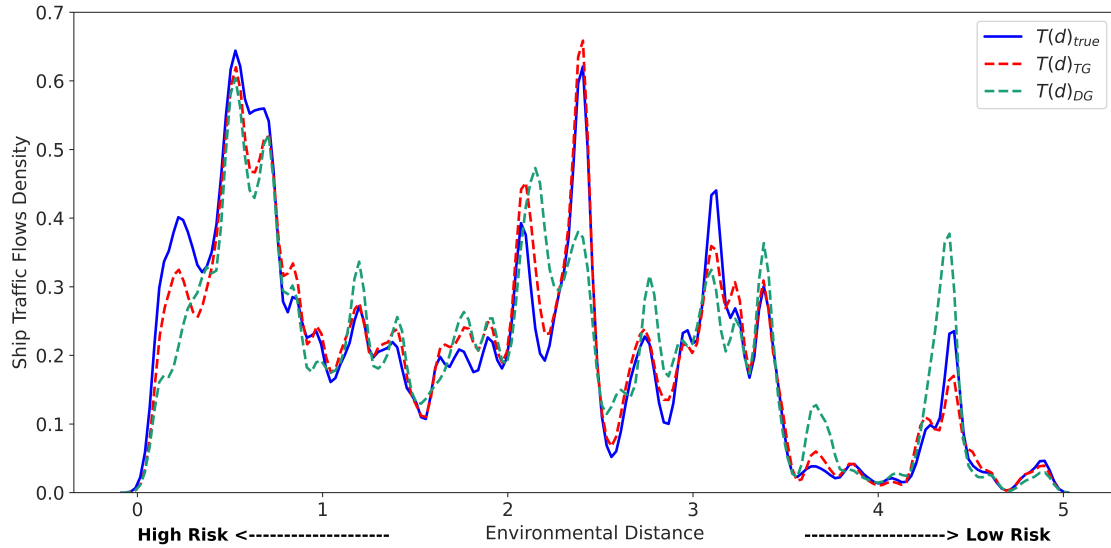


Figure 7. Distribution of environmental distances for shipping flows in 2019. The true shipping flows are represented by the blue curve, while the dashed red and green curves depict the predictions from the Transformer Gravity (TG) and Deep Gravity (DG) models, respectively. The x-axis measures the environmental distance; smaller values indicate higher risk levels, and larger values indicate lower risks.

consistency between $T(d)_{TG}$ and $T(d)_{true}$ is more pronounced where the environmental distance is greater, implying a lower risk of invasion. Conversely, when smaller environmental distances indicate a higher invasion risk, the two groups show more discrepancies. Since the distance values in the two groups are calculated from the origin-destination pairs of the same year, these discrepancies can be attributed to the differences between the predicted and the real shipping flows. On the other hand, the Transformer Gravity model contains an important feature, *i.e.*, exportation values, quantifying the annual trading volume between two countries in US dollars. When contributing to the model's predictive performance, the feature value becomes zero and no longer positively associates trade with shipping flows when predicting inner-country shipping activities, and these are usually high-risk routes due to more environmental similarity between the source and destination locations. Further, there may also be critical factors in predicting high-risk shipping connections that remain unexplored, suggesting potential for further studies.

Although there are some discrepancies in the high-risk interval, the evaluation results show an overall low error of 0.208 and a high similarity between the environmental distances scaled according to the predicted and actual shipping flows. This result suggests that the high performance of our Transformer Gravity model for ship traffic flow prediction contributes significantly to representing shipping intensity in BWRA. This has contributed to a more accurate risk assessment for the spread of NIS through ballast water and thus provides a valuable reference for global ballast water risk management in the future.

Discussion

The ability to assess and predict the risks of NIS invasion through ballast water relies heavily on shipping fluxes. In order to improve BWRA, we have introduced a new approach called the Transformer Gravity model. Our Transformer Gravity model is built based on a stack of multi-head attention blocks. It incorporates features originating from the gravity-informed model, including the shipping fluxes, origin and destination locations, and the geographical distance between them. We enriched the feature set by integrating additional factors, including the international bilateral trade information and the graph metrics analyzed from the global shipping network, to enhance the model's capability for predicting ship traffic flows. We have validated our approach through a comprehensive comparison with established gravity models and a range of machine-learning regression techniques to highlight its advancements.

Our findings established the superiority of the Transformer Gravity model across several performance indicators. Notably, the model achieved the highest CPC with minimal variance across different data folds, indicating its robustness and adaptability to new datasets. The best average CPC in the cross-validation set was 0.864 for the 3 and 5-layer models. Besides, the 3-layer one demonstrated the lowest mean error, 0.080, and the highest mean correlation, 0.977. Variations in performance among baseline models highlighted their inadequacies in dealing with diverse data scenarios, thus reinforcing our model's resilience.

Our study has limitations that can be improved with future and further research. For instance, our model tends to be over-optimistic in targeting high-risk ship traffic predictions, and there might be underlying features that can contribute more to forecasting high-risk trips. Seasonality of environmental variables can affect the results of environmental distance calculation, and using environmental data collected from a smaller temporal scale can reflect the evaluated risk more precisely. Our study did not consider ecological barriers that divide ecoregions, which can overestimate the risk of some short-distance trips within the same ecoregions. Also, the change in shipping patterns due to COVID-19 requires further investigation into changes in shipping behavior and their impact on BWRA, which is a concern for future studies.

In summary, the Transformer Gravity model proposed in this study has markedly improved the performance of ship traffic flow forecast, outperforming other gravity-informed models. It has also shown high-performance consistency when applied to different data subsets with various spatio-temporal distributions. Future mobility studies and applications can enhance the model's explainability and transparency by exploring the intrinsic relationships between various features and the flow prediction results. The exploration of such aspects can improve the model's interpretability and help the model's application in domains where a high degree of accuracy is expected on the OD flow representation.

Methods

Connected components: A component is a group of vertices that are connected to each other, and a network that has more than one group of vertices that are not connected is called a non-connected graph. In an arbitrary graph, vertices i and j are in the same component $G' = \{V', E'\}$, $V' \subseteq V$, if and only if

$\{\forall i \in V', \forall j \in V' | d_{ij} < \infty\}$, meaning that it is possible to travel from any vertex i to any vertex j in a finite number of steps, where $d_{ij} : V \times V \rightarrow \mathbb{R}$ is a function that returns the distance between any two vertices⁵⁶. Connected components are defined for undirected graphs but can also be extended to directed graphs, resulting in weakly and strongly connected components, which help in identifying absorbing regions.

Geodesic distance (d_{ij}^E): The geodesic distance, as defined in Equation 12, measures the shortest distance between two vertices $i \in V$ and $j \in V$ on a sphere's surface⁵⁷. This metric incorporates the latitudes ϕ_i and ϕ_j of vertices i and j , the difference Δ_{ij}^λ between their longitudes λ_i and λ_j , and the Earth's radius \mathbf{R} (6,371 km). All values are calculated in radians.

$$d_{ij}^E = \left(\sin(\phi_i) \times \sin(\phi_j) + \cos(\phi_i) \times \cos(\phi_j) \times \cos(\Delta_{ij}^\lambda) \right) \times \mathbf{R} \quad (12)$$

Shortest distance (d_{ij}^N): A path S between two vertices i and j is a sequence of connected vertices $S^n = \langle v_1, v_2, \dots, v_{q-1}, v_q \rangle$, where each consecutive vertex is connected through an edge $\langle S_m^n, S_{m+1}^n \rangle \in E$ for all $m \in [1, |S^n|]$. The shortest directed path d_{ij}^N is obtained by minimizing the weight function $f : E^n \rightarrow \mathbb{R}$, which describes the cost of the paths among all possible paths $\mathbb{S} = \{S^1, S^2, \dots, S^n\}$ between vertices i and j ⁵⁸. The goal is to find the path with the minimum cost, which is determined by the sum of the weights of the edges. The weight is defined as the straight-line distance between the vertices, such as in Equation 13.

$$d_{ij}^N = \min \left(\sum_{m=1}^{|S|-1} f(\langle S_m^n, S_{m+1}^n \rangle), \forall S^n \in \mathbb{S} \right) \quad (13)$$

Closeness centrality (C_C): The Closeness measures how closely a vertex is connected to all the other vertices in a network, as determined by the shortest paths between them (refer to Equation 14). A vertex with higher centrality is considered more central and has a shorter average distance to all other vertices in the network⁵⁹. In a port network, the closeness-central ports are expected to have higher traffic of vessels, providing insight into trading behavior and economic relationships inherent to their country and cities.

$$C_C(i) = \frac{|V| - 1}{\sum_{j=1}^{|V|} d_{ij}^N}, i \neq j \quad (14)$$

Straightness centrality (C_S): This metric measures the straightness of paths connecting vertices i and j . It does so by comparing the deviation of the geodesic distance d_{ij}^E and the shortest path distance d_{ij}^N that links them⁶⁰. A high centrality value indicates the existence of connections with distances close to the geodesic one. When the two distances match, it is the optimal scenario for communication between vertices.

$$C_S(i) = \frac{1}{|V| - 1} \sum_{j=1}^{|V|} \frac{d_{ij}^E}{d_{ij}^N}, i \neq j \quad (15)$$

Betweenness centrality (C_B): The Betweenness identifies how often a particular vertex is present in the shortest paths of a graph. A higher metric value indicates that the vertex is present in a larger number of shortest paths. In Equation 16, $\sigma(u, v)$ represents the number of shortest paths between vertices u and v ,

and $\sigma(u, v|i)$ represents the number of those paths that pass through vertex i . It is worth noting that there is also the *Edge-Betweenness*, which assigns a Betweenness value to each edge in a graph. This variant considers $\sigma(u, v|i)$ as the number of shortest paths between vertices u and v that pass through edge i .

$$C_B(i) = \sum_{\langle u,v \rangle \in V} \frac{\sigma(u, v|i)}{\sigma(u, v)}, u \neq v \quad (16)$$

PageRank (P_{ij}): The PageRank is based on a mathematical model known as the stochastic Markovian process. This model defines a probability distribution over a set of states, where the probability of transitioning from one state to another is solely correlated with the state immediately preceding it:

$$P_{ij} = \mathbf{P}(X_{n+1} = j | X_n = i) \quad (17)$$

The algorithm assesses the significance of a vertex with respect to the significance of the vertices that are linked to it. This way, it measures the vertex contribution based on the number of outgoing edges each adjacent vertex has, ensuring the uniqueness of the edge. To determine vertex importance, the algorithm calculates the stationary transition probability matrix. The values obtained from this calculation indicate the significance of the vertices based on their access probability. Equation 18 illustrates the stationary matrix, where $\pi^{(n)}$ denotes the probability matrix at time n , and \mathbf{P} is the transition probability matrix.

$$\pi^{(n-1)}\mathbf{P} = \pi^{(n)} \quad (18)$$

Features information: Features incorporated in this study are listed in Table 3, including shipping fluxes, distances, international trade volume, and the graph metrics computed from the global shipping network.

Feature name	Feature information
<i>Original port fluxes</i>	Shipping fluxes at source port
<i>Destination region fluxes</i>	Total shipping fluxes at the destination geographical region
<i>Distance</i>	Geodesic distance between the source port to the destination region center
<i>Exportation volume</i>	Exportation volume in US dollars from source to destination
<i>Betweenness centrality</i>	Betweenness centrality at the original port and the median betweenness centrality in the destination region
<i>Closeness centrality</i>	Closeness centrality at the original port and the median closeness centrality in the destination region
<i>Page rank</i>	Page rank at the original port and the median page rank in the destination region

Table 3. Detailed information of features used in Transformer Gravity and other gravity-informed models.

References

1. Group, S. R. Container shipping - statistics & facts. <https://www.statista.com/topics/1367/container-shipping/#topicOverview> (2022).
2. Barry, S. C. *et al.* Ballast water risk assessment: Principles, processes, and methods. *ICES J. Mar. Sci.* **65**, 121–131, DOI: [10.1093/icesjms/fsn004](https://doi.org/10.1093/icesjms/fsn004) (2008).
3. Gollasch, S. & Leppäkoski, E. *Initial risk assessment of alien species in nordic coastal waters* (Nordic Council of Ministers, Copenhagen, Denmark, 1999).
4. Clarke, C., Facility, G. E., Organization, I. M., Programme, G. B. W. M. & Programme, U. N. D. *Ballast Water Risk Assessment: Port of Khark Island, Islamic Republic of Iran : Final Report*. GloBallast Monograph Series (Programme Coordination Unit, Global Ballast Water Management Programme, 2003).
5. Awad, A. & Programme, G. B. W. M. *Ballast Water Risk Assessment: Port of Saldanha Bay Republic of South Africa : November 2003 : Final Report*. GloBallast Monograph Series (International Maritime Organization, 2004).
6. Keller, R. P., Drake, J. M., Drew, M. B. & Lodge, D. M. Linking environmental conditions and ship movements to estimate invasive species transport across the global shipping network. *Divers. Distributions* **17**, 93–102, DOI: [10.1111/j.1472-4642.2010.00696.x](https://doi.org/10.1111/j.1472-4642.2010.00696.x) (2011).
7. David, M., Gollasch, S. & Leppäkoski, E. Risk assessment for exemptions from ballast water management – The Baltic Sea case study. *Mar. Pollut. Bull.* **75**, 205–217, DOI: [10.1016/j.marpolbul.2013.07.031](https://doi.org/10.1016/j.marpolbul.2013.07.031) (2013).
8. Seebens, H., Schwartz, N., Schupp, P. J. & Blasius, B. Predicting the spread of marine species introduced by global shipping. *Proc. Natl. Acad. Sci.* **113**, 5646–5651, DOI: [10.1073/pnas.1524427113](https://doi.org/10.1073/pnas.1524427113) (2016).
9. Song, R., Tavakoli, Y., Bailey, S. A. & Soares, A. A temporal assessment of risk of non-indigenous species introduction by ballast water to Canadian coastal waters based on environmental similarity. *Biol. Invasions* **25**, 1991–2005, DOI: [10.1007/s10530-023-03019-1](https://doi.org/10.1007/s10530-023-03019-1) (2023).
10. Saebi, M. *et al.* Higher-order patterns of aquatic species spread through the global shipping network. *PLOS ONE* **15**, 1–24, DOI: [10.1371/journal.pone.0220353](https://doi.org/10.1371/journal.pone.0220353) (2020).
11. Bradie, J. N. & Bailey, S. A. A decision support tool to prioritize ballast water compliance monitoring by ranking risk of non-indigenous species establishment. *J. Appl. Ecol.* **58**, 587–595, DOI: [10.1111/1365-2664.13822](https://doi.org/10.1111/1365-2664.13822) (2021).
12. Seebens, H., Gastner, M. T. & Blasius, B. The risk of marine bioinvasion caused by global shipping. *Ecol. Lett.* **16**, 782–790, DOI: [10.1111/ele.12111](https://doi.org/10.1111/ele.12111) (2013).

13. Etemad, M., Soares, A., Mudroch, P., Bailey, S. A. & Matwin, S. Developing an advanced information system to support ballast water management. *Manag. Biol. Invasions* **13**, 68–80, DOI: [10.3391/mbi.2022.13.1.04](https://doi.org/10.3391/mbi.2022.13.1.04) (2022).
14. Center, S. E. R. National Ballast Information Clearinghouse (NBIC) Database. <https://nbic.si.edu/database/>. Accessed: 2023-09-30.
15. Kaluza, P., Kölzsch, A., Gastner, M. T. & Blasius, B. The complex network of global cargo ship movements. *J. The Royal Soc. Interface* **7**, 1093–1103, DOI: [10.1098/rsif.2009.0495](https://doi.org/10.1098/rsif.2009.0495) (2010).
16. Haranwala, Y. J., Spadon, G., Renso, C. & Soares, A. A data augmentation algorithm for trajectory data. In *1st ACM SIGSPATIAL International Workshop on Methods for Enriched Mobility Data: Emerging issues and Ethical perspectives 2023 (EMODE '23)*, 5, DOI: [10.1145/3615885.3628008](https://doi.org/10.1145/3615885.3628008) (ACM, New York, NY, USA, New York, NY, USA, 2023).
17. Spadon, G. *et al.* Building a safer maritime environment through multi-path long-term vessel trajectory forecasting. *arXiv* (2023). [2310.18948](https://arxiv.org/abs/2310.18948).
18. Spadon, G., Ferreira, M. D., Soares, A. & Matwin, S. Unfolding ais transmission behavior for vessel movement modeling on noisy data leveraging machine learning. *IEEE Access* **11**, 18821–18837, DOI: [10.1109/ACCESS.2022.3197215](https://doi.org/10.1109/ACCESS.2022.3197215) (2023).
19. Nguyen, D., Vadaine, R., Hajduch, G., Garello, R. & Fablet, R. Geotracknet - A maritime anomaly detector using probabilistic neural network representation of AIS tracks and A contrario detection. *IEEE Transactions on Intell. Transp. Syst.* **23**, 5655–5667, DOI: [10.1109/TITS.2021.3055614](https://doi.org/10.1109/TITS.2021.3055614) (2022).
20. Nguyen, D. & Fablet, R. TrAISformer-a generative transformer for AIS trajectory prediction. *CoRR abs/2109.03958* (2021). [2109.03958](https://arxiv.org/abs/2109.03958).
21. Ferreira, M. D., Spadon, G., Soares, A. & Matwin, S. A semi-supervised methodology for fishing activity detection using the geometry behind the trajectory of multiple vessels. *Sensors* **22**, 6063, DOI: [10.3390/s22166063](https://doi.org/10.3390/s22166063) (2022).
22. Isaac Newton, I. Bernard Cohen & Anne Whitman. Proposition 75, Theorem 35. In *The Principia: Mathematical Principles of Natural Philosophy, 3rd Edition (1726)*, 956 (University of California Press, 1999).
23. Zipf, G. K. The P1 P2/D Hypothesis: On the Intercity Movement of Persons. *Am. Sociol. Rev.* **11**, 677–686, DOI: [10.2307/2087063](https://doi.org/10.2307/2087063) (1946).
24. Jung, W.-S., Wang, F. & Stanley, H. E. Gravity model in the Korean highway. *Europhys. Lett.* **81**, 48005, DOI: [10.1209/0295-5075/81/48005](https://doi.org/10.1209/0295-5075/81/48005) (2008).
25. Ventura, P. C., Aleta, A., Rodrigues, F. A. & Moreno, Y. Modeling the effects of social distancing on the large-scale spreading of diseases. *Epidemics* **38**, 100544, DOI: <https://doi.org/10.1016/j.epidem.2022.100544> (2022).

26. Kramer, A. M. *et al.* Spatial spread of the west africa ebola epidemic. *Royal Soc. Open Sci.* **3**, 160294, DOI: [10.1098/rsos.160294](https://doi.org/10.1098/rsos.160294) (2016).
27. Van Bergeijk, P. A. & Brakman, S. *The Gravity Model in International Trade: Advances and Applications* (Cambridge University Press, 2010).
28. González, M. C., Hidalgo, C. A. & Barabási, A.-L. Understanding individual human mobility patterns. *Nature* **453**, 779–782, DOI: [10.1038/nature06958](https://doi.org/10.1038/nature06958) (2008).
29. Ducruet, C., Itoh, H. & Berli, J. Urban gravity in the global container shipping network. *J. Transp. Geogr.* **85**, 102729, DOI: [10.1016/j.jtrangeo.2020.102729](https://doi.org/10.1016/j.jtrangeo.2020.102729) (2020).
30. Beyer, R. M., Schewe, J. & Lotze-Campen, H. Gravity models do not explain, and cannot predict, international migration dynamics. *Humanit. Soc. Sci. Commun.* **9**, 1–10, DOI: [10.1057/s41599-022-01067-x](https://doi.org/10.1057/s41599-022-01067-x) (2022).
31. Song, C., Qu, Z., Blumm, N. & Barabási, A.-L. Limits of Predictability in Human Mobility. *Science* **327**, 1018–1021, DOI: [10.1126/science.1177170](https://doi.org/10.1126/science.1177170) (2010).
32. Simini, F., González, M. C., Maritan, A. & Barabási, A.-L. A universal model for mobility and migration patterns. *Nature* **484**, 96–100, DOI: [10.1038/nature10856](https://doi.org/10.1038/nature10856) (2012).
33. Masucci, A. P., Serras, J., Johansson, A. & Batty, M. Gravity versus radiation models: On the importance of scale and heterogeneity in commuting flows. *Phys. Rev. E: Stat. Physics, Plasmas, Fluids, Relat. Interdiscip. Top.* **88**, 022812, DOI: [10.1103/PhysRevE.88.022812](https://doi.org/10.1103/PhysRevE.88.022812) (2013).
34. Ren, Y., Ercsey-Ravasz, M., Wang, P., González, M. C. & Toroczkai, Z. Predicting commuter flows in spatial networks using a radiation model based on temporal ranges. *Nat. Commun.* **5**, 5347, DOI: [10.1038/ncomms6347](https://doi.org/10.1038/ncomms6347) (2014).
35. Mazzoli, M. *et al.* Field theory for recurrent mobility. *Nat. Commun.* **10**, 3895, DOI: [10.1038/s41467-019-11841-2](https://doi.org/10.1038/s41467-019-11841-2) (2019).
36. J. Wang, J. Ji, Z. Jiang & L. Sun. Traffic Flow Prediction Based on Spatiotemporal Potential Energy Fields. *IEEE Transactions on Knowl. Data Eng.* 1–14, DOI: [10.1109/TKDE.2022.3221183](https://doi.org/10.1109/TKDE.2022.3221183) (2022).
37. Rodrigues-Jr, J. F., Spadon, G., Brandoli, B. & Amer-Yahia, S. Patient trajectory prediction in the Mimic-III dataset, challenges and pitfalls. *CoRR* **abs/1909.04605** (2019). [1909.04605](https://arxiv.org/abs/1909.04605).
38. Rodrigues-Jr, J. F., Gutierrez, M. A., Spadon, G., Brandoli, B. & Amer-Yahia, S. Lig-doctor: Efficient patient trajectory prediction using bidirectional minimal gated-recurrent networks. *Inf. Sci.* **545**, 813–827, DOI: [10.1016/j.ins.2020.09.024](https://doi.org/10.1016/j.ins.2020.09.024) (2021).
39. Spadon, G. *et al.* Pay attention to evolution: Time series forecasting with deep graph-evolution learning. *IEEE Transactions on Pattern Analysis Mach. Intell.* **44**, 5368–5384, DOI: [10.1109/TPAMI.2021.3076155](https://doi.org/10.1109/TPAMI.2021.3076155) (2022).

40. Brandoli, B. *et al.* Aircraft fuselage corrosion detection using artificial intelligence. *Sensors* **21**, DOI: [10.3390/s21124026](https://doi.org/10.3390/s21124026) (2021).
41. Simini, F., Barlacchi, G., Luca, M. & Pappalardo, L. A Deep Gravity model for mobility flows generation. *Nat. Commun.* **12**, 6576, DOI: [10.1038/s41467-021-26752-4](https://doi.org/10.1038/s41467-021-26752-4) (2021).
42. Spadon, G., Carvalho, A. C. d., Rodrigues-Jr, J. F. & Alves, L. G. Reconstructing commuters network using machine learning and urban indicators. *Sci. reports* **9**, 11801, DOI: [10.1038/s41598-019-48295-x](https://doi.org/10.1038/s41598-019-48295-x) (2019).
43. The Growth Lab at Harvard University. International trade data (SITC, rev. 2), DOI: [10.7910/DVN/H8SFD2](https://doi.org/10.7910/DVN/H8SFD2) (2019).
44. Vaswani, A. *et al.* Attention is all you need. In Guyon, I. *et al.* (eds.) *Advances in Neural Information Processing Systems*, vol. 30 (Curran Associates, Inc., 2017).
45. Carlini, E. *et al.* Understanding evolution of maritime networks from automatic identification system data. *GeoInformatica* **26**, 479–503, DOI: [10.1007/s10707-021-00451-0](https://doi.org/10.1007/s10707-021-00451-0) (2022).
46. National Geospatial-Intelligence Agency (NGA). World Port Index (Pub 150). <https://msi.nga.mil/Publications/WPI> (2019).
47. Page, L., Brin, S., Motwani, R. & Winograd, T. The PageRank Citation Ranking : Bringing Order to the Web. In *The Web Conference* (1999). <https://www.eecs.harvard.edu/~michaelm/CS222/pagerank.pdf>.
48. Gent Halili. Searoute-py: A python package to calculate the shortest sea route between two points on Earth. <https://github.com/genthalili/searoute-py> (2022).
49. Crucitti, P., Latora, V. & Porta, S. Centrality measures in spatial networks of urban streets. *Phys. Rev. E* **73**, 036125, DOI: [10.1103/PhysRevE.73.036125](https://doi.org/10.1103/PhysRevE.73.036125) (2006).
50. Tu, N., Adiputranto, D., Fu, X. & Li, Z.-C. Shipping network design in a growth market: The case of Indonesia. *Special Issue on China's Belt Road Initiative* **117**, 108–125, DOI: [10.1016/j.tre.2017.10.001](https://doi.org/10.1016/j.tre.2017.10.001) (2018).
51. Codes for the representation of names of countries and their subdivisions - Part 2: Country subdivision code. Standard, International Organization for Standardization, Geneva, Switzerland (2020). <https://www.iso.org/standard/72483.html>.
52. Luca, M., Barlacchi, G., Lepri, B. & Pappalardo, L. A Survey on Deep Learning for Human Mobility. *ACM Comput. Surv.* **55**, 7:1–7:44, DOI: [10.1145/3485125](https://doi.org/10.1145/3485125) (2021).
53. Lenormand, M., Bassolas, A. & Ramasco, J. J. Systematic comparison of trip distribution laws and models. *J. Transp. Geogr.* **51**, 158–169, DOI: [10.1016/j.jtrangeo.2015.12.008](https://doi.org/10.1016/j.jtrangeo.2015.12.008) (2016).

54. Barbosa, H. *et al.* Human mobility: Models and applications. *Phys. Reports* **734**, 1–74, DOI: [10.1016/j.physrep.2018.01.001](https://doi.org/10.1016/j.physrep.2018.01.001) (2018).
55. Bailey, S. A., Bradie, J. N., Ogilvie, D. & Mudroch, P. Global port environmental data used for environmental distance calculations [Dataset], DOI: [10.5061/dryad.69p8cz906](https://doi.org/10.5061/dryad.69p8cz906) (2020).
56. Cormen, T., Leiserson, C., Rivest, R. & Stein, C. *Introduction To Algorithms* (MIT Press, 2001).
57. Konstantopoulos, T. *Introduction to projective geometry*. September (Dover Publications, 2012).
58. Van Steen, M. *Graph Theory and Complex Networks: An Introduction* (Maarten van Steen, 2010).
59. Kas, M., Carley, K. M. & Carley, L. R. Incremental Closeness Centrality for Dynamically Changing Social Networks. In *Proceedings of the 2013 IEEE/ACM International Conference on Advances in Social Networks Analysis and Mining - ASONAM'13*, DOI: [10.1145/2492517.2500270](https://doi.org/10.1145/2492517.2500270) (Association for Computing Machinery (ACM), 2013).
60. Vragović, I., Louis, E. & Díaz-Guilera, A. Efficiency of informational transfer in regular and complex networks. *Phys. Rev. E - Stat. Nonlinear, Soft Matter Phys.* **71**, 036122, DOI: [10.1103/PhysRevE.71.036122](https://doi.org/10.1103/PhysRevE.71.036122) (2005).

Acknowledgments

This research was partially funded by the Natural Sciences and Engineering Research Council of Canada (NSERC), Grant number RGPIN-2022-03909; Sao Paulo State Research Foundation (FAPESP), Grant number 2016/17078-0 and 2022/12374-1; the Institute for Big Data Analytics (IBDA) and the Ocean Frontier Institute (OFI) at Dalhousie University, Halifax - NS, Canada; and further funded by the Canada First Research Excellence Fund (CFREF), the Canadian Foundation for Innovation MERIDIAN cyberinfrastructure. We thank all funding sources and *Spire* for providing the vessel trajectory dataset. We also thank Sarah Bailey, from the Great Lakes Laboratory for Fisheries and Aquatic Sciences, Fisheries and Oceans, Dartmouth – NS, Canada, for reviewing and sharing her thoughts about this paper.

Author contributions statement

Conceptualization, R.S. and G.S.; methodology, R.S., G.S. and A.S.; validation, R.S., G.S., and A.S.; formal analysis, R.S., and G.S.; data modeling, R.S. and G.S.; data curation, R.S., G.S., and A.S.; writing — original draft preparation, R.S. and G.S.; writing — review and editing, all authors; visualization, R.S.; supervision, R.P., S.M., and A.S.; project administration, G.S. and A.S.; funding acquisition, R.P., S.M., A.S.; All authors have read and agreed to the published version of the manuscript.

Competing interests

The authors declare no competing interests.